Supporting Information

Agnew et al. 10.1073/pnas.1106341108

SI Materials and Methods

Protein Production and Purification. A series of truncated forms of *Moraxella catarrhalis (Mx)* ubiquitous surface protein A1 (UspA1) from strain MX2 ATCC 25238 (Fig. S1), each containing the head domain region, were cloned into the pOPINE expression vector (Oxford Protein Production Facility) and transformed into Rosetta 2 (DE3) pLysS *Escherichia coli* for expression. A 10-mL culture was inoculated from a frozen stock and grown overnight at 37 °C. Expression was induced with 1 mM IPTG and cell growth continued at 20 °C for 20 h. Cells were harvested by centrifugation, the cell pellet was resuspended in buffer A [50 mM Tris (pH 8), 500 mM NaCl, 10% vol/vol glycerol, and 20 mM imidazole] with one protease inhibitor tablet (Roche) and DNAse I (Sigma). The protein was liberated by sonication and cell debris removed by centrifugation. The supernatant was applied to a preequilibrated 5 mL HiTrap Ni column (GE Healthcare) and recombinant protein eluted in a gradient of buffer B [50 mM Tris (pH 8), 500 mM NaCl, 10% vol/vol glycerol, and 1 M imidazole]. Pooled fractions were further subjected to gel filtration on a HiLoad 16/60 superdex 200 (GE Healthcare) equilibrated in 20 mM Tris (pH 8) and 500 mM NaCl. The recombinant proteins were confirmed by N-terminal sequencing and mass spectrometry.

Recombinant human fibronectin (Fn) constructs $FnIII_{12–15}$, $FnIII_{12\text{-IIICS-}15}$, $FnIII_{6–10}$ (Fig. S1) were a kind gift from Martin Humphries (University of Manchester, United Kingdom) and were prepared as described previously (1). Two- and three-domain constructs derived from $FnIII_{12–15}$ (Fig. S1) were cloned into the pOPINF expression vector, and $FnIII_{6–10}$ into vector popiNE. Expression and purification followed the protocols developed for the truncated forms *Mx* UspA1 (as described above).

Crystallization and Structure Determination. Crystallization of each of the UspA1 constructs was attempted. Crystals were successfully obtained starting from the $UspA1^{(42–366)}$ protein by vapor diffusion in sitting drops at 18 °C, by mixing protein solution (7 mg/mL) (200 nL) and well solution (200 nL) and equilibrating against a 60-μL reservoir containing 0.2 M ammonium sulphate, 0.2 M Tris (pH 8.5), 12% PEG 8000. Crystals were also obtained from the $UspA1^{(42–345)}$ construct by the hanging drop method with protein solution (7.5 mg/mL) (1 μL) against well solution (1 μL) with a reservoir buffer of 0.1 M MES (pH 6.5), 0.2 M sodium dihydrogen phosphate, 0.2 M potassium dihydrogen phosphate, and 2 M sodium chloride. Initial crystals were improved for diffraction experiments by streak seeding into a preequilibrated drop with a reservoir buffer of 0.1 M MES (pH 6.5), 0.2 M sodium dihydrogen phosphate, 0.2 M potassium dihydrogen phosphate, and 1 M sodium chloride. All crystals were cryoprotected with 30% glycerol before flash-freezing into liquid nitrogen.

Diffraction data were collected at the Diamond Light Source (beamlines IO2 and IO4) and were processed with HKL2000 (2) and subsequently manipulated with the CCP4 suite of crystallographic software (3). The data for crystals derived from the $UspA1^{(42–366)}$ construct initially appeared to belong to the space group $P6_3$ with one $UspA1^{(42–366)}$ monomer in the asymmetric unit and a crystallographic threefold symmetry axis running down the center of the trimer, but could not be fully refined in this space group. The structure was eventually refined in the space group $P2_1$ with the three molecules of the trimer making up the asymmetric unit. The structure of $UspA1^{(42–366)}$ was solved through a combination of molecular replacement and experimental phasing from bromide soaks using programs PHASER (4) and SHELX (5). The successful molecular replacement strategy used poly-Ala fragments of three trimeric structures as search models: residues 65–165 of the head domain of *Yersinia enterocolitica* YadA (Protein Data Bank ID 1P9H) with sequence identity of 28%; residues 104–163 (loop 123–129 removed) of the neck domain of *Burkholderia pseudomallei* XadA (3LAA) with sequence identity of 55%; and residues 987–1022 of the coiled-coil domain of *Haemophilus influenzae* Hia (3EMO) with 44% sequence identity. Promising solutions were obtained using just the head and coiled-coil motifs as search models, but the phases were insufficient to assign the correct amino acid sequence. It was only when the three separate domains were used together in molecular replacement that the sequence could be correctly placed, confirmed by the bromide anomalous signal, and the structure fully refined. The structure was refined with iterative cycles of manual model building using COOT (6), restrained refinement with REFMAC5 (7), and density improvement with ARP/wARP (8) as the correct sequence was gradually built into the improving electron density maps. The structure of crystals of $UspA1^{(42–345)}$ was subsequently solved in the space group $P6_3$ with one trimer in the asymmetric unit by molecular replacement using the structure from the $UspA1^{(42–366)}$ crystals (which contained residues 153–366; see *Results*) with additional sheets being built in to the resulting electron density using COOT and refined as above. Data collection and final refinement statistics for both structures are summarized in Table S1.

Binding Studies. The interactions of UspA1 and Fn fragments were studied using the following techniques.

Dot immunoblot assays. Binding of the UspA1 fragments to the Fn constructs was assessed by dot immunoblotting essentially as described previously (9, 10). Briefly, the UspA1 fragments $UspA1^{(42–345)}$, $UspA1^{(42–366)}$, or $UspA1^{(42–387)}$ (1 μg per dot) were applied to nitrocellulose and nonspecific binding sites were blocked using 5% milk in phosphate-buffered saline containing 0.05% Tween 20 (milk-PBST). Nitrocellulose strips were overlaid with the following Fn constructs (each at 3 μg/mL): $FnIII_{6–10}$, $FnIII_{12–15}$, $FnIII_{12\text{-IIICS-}15}$, $FnIII_{12–13}$, $FnIII_{13–14}$, $FnIII_{12,13,14}$, or $FnIII_{13,14,15}$ for 1 h at room temperature. Binding of Fn constructs was detected by using rabbit antifibronectin polyclonal antibody (Sigma-Aldrich), followed by a goat anti-rabbit IgG antibody conjugated to alkaline phosphatase (Sigma-Aldrich). Blots were developed with nitroblue tetrazolium and 5-bromo-4-chloro-3-indoylphosphate substrates. To monitor any nonspecific binding, control strips containing UspA1 fragments were overlaid with antifibronectin and anti-rabbit antibodies only, and developed as above. Relative binding was quantified by densitometric analysis using the National Institutes of Health Scion Image program. Commercially available full-length human cellular (Sigma-Aldrich) or plasma fibronectin (Roche) were used as positive controls.

Enzyme-linked immunosorbent assay. Ninety-six-well ELISA plates (Dynex) were coated overnight at 4 °C with $UspA1^{(42–366)}$ fragment (1 μg per well) in coating buffer (50 mM carbonate/bicarbonate buffer, pH 9.6). Nonspecific binding sites were blocked in milk-PBST. Direct-binding ELISA was performed, by the addition of Fn constructs (3 μg/mL) for 1 h at room temperature. The bound Fn constructs were detected as above, the plates developed using p-nitrophenyl phosphate substrate (Sigma-Aldrich) and absorbance measured at 405 nm. Human cellular or plasma fibronectin were again used as positive controls.

The results from these studies confirmed that, under a variety of solution conditions, full-length Fn bound strongly to the UspA1$^{(42–366)}$ fragment, whereas binding was diminished with UspA1$^{(42–345)}$ and UspA1$^{(42–387)}$ (Fig. S3 *A* and *B*). Blots were then extended to truncated forms of Fn, using the UspA1$^{(42–366)}$ construct and both immunoblotting and ELISA techniques (Fig. S3*C*). In these studies, the binding of the central Fn fragment FnIII$_{6–10}$, containing the integrin-binding site, to UspA1$^{(42–366)}$ was weak and is unlikely to play a role in the UspA1-Fn interaction. The binding of FnIII$_{12–15}$ and FnIII$_{12\text{-IICS-}15}$ fibronectin fragments to UspA1$^{(42–366)}$ was comparable to the binding levels of full-length human cellular or plasma fibronectin, clearly indicating that the UspA1 adhesin targets a C-terminal part within the fibronectin, containing the heparin-binding site. Strong interactions between FnIII$_{13–14}$ or FnIII$_{13,14,15}$ and UspA1$^{(42–366)}$ were observed, whereas binding was diminished with construct FnIII$_{14–15}$ indicating that FnIII$_{14}$ or FnIII$_{15}$ were not involved in the interaction between Fn and UspA1 molecules. Immunodotblotting and ELISA binding data indicated that FnIII$_{13}$ plays a potentially key role in the interaction between Fn fragments and UspA1$^{(42–366)}$.

Plasmon resonance. For further quantitative comparison of binding, a BIAcore T100 instrument (Biacore) was used to perform binding kinetics experiments. The UspA1 head domain constructs were coupled to CM5 sensor chip using the N-(3-dimethylaminopropyl)-N′-ethylcarbodiimide and N-hydroxysuccinimide amine-coupling kit, yielding approximately 150–500 resonance units each. The recombinant protein *Plasmodium falciparum* lactate dehydrogenase (*Pf*LDH) (11) and a blank cell were both used as controls. The analytes were prepared by size exclusion chromatography directly into the surface plasmon resonance (SPR) running buffer ([10 mM Hepes, 150 mM NaCl, 3.4 mM EDTA, and 0.005% surfactant P20 (pH 7.4)]. Interaction analysis was performed at 25 °C. Ten serial dilutions of each analyte (ranging from approximately 100 μM to 100 nM) were injected sequentially at 10 μL/min flow rate. Between each analyte, surfaces were regenerated using glycine buffer pH 3.0. Results were analyzed using BIAevaluation 3.1, Microsoft Excel, and Origin 6.1. The equilibrium binding constant (K_d) values were calculated using a nonlinear curve fit ($y = (P_1x)/(P_2 + x)$). Experiments to analyze the competition between fibronectin constructs and increasing concentrations of heparin (Sigma-Aldrich) were also performed.

The SPR results mirrored the data from the dot-blot assays. Relative to UspA1$^{(42–366)}$, truncated constructs UspA1$^{(42–345)}$, and UspA1$^{(42–387)}$ displayed weak association to the Fn constructs ($K_d > 500$ μM). UspA1$^{(42–366)}$ bound weakly to FnIII$_{14,15}$, but with relatively high affinity ($K_d \sim 5$–43 μM) to all other Fn constructs tested (FnIII$_{12,13}$, FnIII$_{13,14}$, FnIII$_{12,13,14}$, FnIII$_{13,14,15}$, FnIII$_{12–15}$) (Fig. S4). These interactions were characterized by very fast on and off rates, from which it was not possible to directly determine the kinetic parameters (k_{off}/k_{on}). Dissociation constants were therefore calculated from the equilibrium binding responses (Table S2).

Small-Angle X-Ray Scattering (SAXS) Analysis. SAXS data of the FnIII$_{12–15}$/UspA1$^{(42–366)}$ complex were collected at the Diamond Light Source (beamline I22) at a wavelength of $\lambda = 0.1$ nm and sample-to-detector distance of 2.5 m. Two sample concentrations were measured: 2.2 and 1.65 mg/mL. Samples were exposed for 200 frames of 1 s. Each frame was sector-integrated with in-house beamline software. Inspection of the scattering patterns indicated that the first 10 frames in each dataset were free from the effects of radiation damage, therefore these frames were averaged. There was no evidence of concentration-dependent effects, so data from the 2.2 mg/mL sample was used for further analysis. Buffer scattering was subtracted using PRIMUS (12). The particle distance distribution function, $p(r)$, maximum intraparticale dimension, D_{max}, and the radius of gyration, R_g, were calculated using GNOM (13). The shape of the protein was evaluated using DAMMIF (14). Fifteen simulations were performed and the resulting structures were filtered and averaged in DAMAVER (15).

Reconstructions of the FnIII$_{12–15}$/UspA1$^{(42–366)}$ complex were performed with SASREF (Petoukov and Svergun 2005) using the following components: UspA1$^{(42–366)}$, FnIII$_{12–14}$, and FnIII$_{15}$. UspA1$^{(42–366)}$ was a composite model generated from the crystal structures of UspA1$^{(42–345)}$ and UspA1$^{(42–366)}$; FnIII$_{12–14}$ was taken from the FnIII$_{12–15}$ crystal structure (1FNH, ref. 1); FnIII$_{15}$ was a model constructed due to the absence of electron density for this domain in the FnIII$_{12–15}$ crystal structure. A minimal contact restraint was imposed to take account of the results of binding studies. The restraint was satisfied if any C^{α} atom of FnIII$_{13}$ was within 6 Å of any C^{α} atom of UspA1$^{(42–366)}$.

Due to the moderate affinity ($K_d \sim 5$ μM) of the complex, the OLIGOMER software (Svergun and Konarev, http://www.embl-hamburg.de/biosaxs/manual_oligomer.html) was also used to fit the theoretical scattering from when a variable mixture of the UspA1$^{(54–372)}$-Fn$_{12–15}$ complex and each of its components to the observed scattering data (Fig. S5). The ratio of volume fractions predicted by OLIGOMER was 87.5% complex and 12.5% noncomplexed components. This ratio is close to that expected (80% complex) from the measured K_d. From the figure and χ values it can be seen that inclusion of the noncomplexed components has little impact on the goodness-of-fit to the experimental scattering data.

Atomic Force Microscopy. The mechanical properties of UspA1 at the outer *Mx* surface were tested by using a newly developed lateral molecular-force microscope (LMFM) (16). This instrument makes use of Si_3N_4 vertically oriented cantilevers (Movie S1). The spring constant of the cantilevers used in this study was 2.4 pN/nm ± 15% and the cross-section was 1 μm ± 10%. To investigate the stiffness of UspA1, we used softer cantilevers with the same cross-section but double the length long, resulting in a stiffness of 2.7 pN/nm ± 15%. The vertical geometry allows nanometer-precision control of the distance between the cantilever tip and surface containing *Mx*. The detection system measures the lateral displacement of the cantilever tip with 1-nm precision. The LMFM was used to investigate overall conformational changes and adhesive properties of the UspA1 when expressed on the bacterial cell surface, and changes in these associated with the binding of the UspA1 receptors, fibronectin, and carcinoembryonic antigen-related cell adhesion molecule 1 (CEACAM1).

Bacteria from strains MX2 ATCC 25238 and 035E, grown as described in previous studies (17), were suspended in PBS and deposited onto glass coverslips by incubation for 24 h. Each coverslip was then mounted on the sample stage of the LMFM and single bacteria were detected optically using total internal reflection illumination (16). Because of the small cross-section of the cantilevers, it is possible to select and probe individual bacteria. A sinusoidal sideways movement was imparted to the sample stage in order to gently push a single bacterium against the cantilever. The position of the bacterium was adjusted to produce a maximum deflection of the cantilever of between 50 and 300 nm. The sample stage was designed to allow small volumes of solution to be directly added while the bacterial interaction with the cantilever is monitored. The position of the contact between the bacterium and the cantilever and the maximum deflection of the cantilever were monitored on the addition of PBS buffer, control protein *Pf*LDH, CEACAM1, and FnIII$_{12–14}$. Changes in the contact positions reflect changes in the size of the bacterium.

Molecular Modeling. Homology models were constructed for the regions of UspA1 not covered by the available crystal structures. The crystal structure of *H. influenzae* Hia trimeric autotransporter residues 992–1098 (18) was used as a template for

UspA1$^{(762–863)}$ which includes the integral membrane domain and C-terminal coiled-coil region. The crystal structure of UspA1$^{(527–665)}$ (19) was used as a template for the missing coiled-coil sections, UspA1$^{(367–526)}$ and UspA1$^{(666–761)}$. A composite structure of UspA1$^{(42–366)}$ was assembled from the two crystal structures reported in this study and combined with the homology models and the UspA1$^{(527–665)}$ crystal structure to form a complete model of UspA1. Modeling of the individual sections and refinement of the overall model was achieved with MODELLER (20), and other molecular modeling manipulations were performed with COOT (6). The stereochemistry of the final model was assessed with MOLPROBITY (21): 99% of residues lay in the most favored regions of the Ramachandran plot, and the overall Molprobity score was in the 66th percentile of crystallographic structures determined at approximately 2-Å resolution.

In order to model the proposed bending of UspA1 upon binding to CEACAM1, a snapshot of a UspA1$^{(666–761)}$–CEACAM1 molecular dynamics simulation (19) was substituted for the UspA1$^{(666–761)}$ section of the full UspA1 model. The snapshot was selected as the point of the molecular dynamics trajectory at which UspA1$^{(666–761)}$ was maximally bent.

1. Sharma A, Askari JA, Humphries MJ, Jones EY, Stuart DI (1999) Crystal structure of a heparin- and integrin-binding segment of human fibronectin. *EMBO J* 18:1468–1479.
2. Otwinowski Z, Minor W (1997) Processing of X-ray diffraction data collected in oscillation mode. *Methods Enzymol* 276:307–326.
3. Collaborative Computing Project No. 4 (1994) The CCP4 suite: Programs for protein crystallography. *Acta Crystallogr D Biol Crystallogr* 50:760–763.
4. McCoy AJ, Grosse-Kunstleve RW, Storoni LC, Read RJ (2005) Likelihood-enhanced fast translation functions. *Acta Crystallogr D Biol Crystallogr* 61:458–464.
5. Sheldrick G (2010) Experimental phasing with SHELXC/D/E: Combining chain tracing with density modification. *Acta Crystallogr D Biol Crystallogr* 66:479–485.
6. Emsley P, Cowtan K (2004) Coot: Model-building tools for molecular graphics. *Acta Crystallogr D Biol Crystallogr* 60:2126–2132.
7. Murshudov GN, Vagin AA, Dodson EJ (1997) Refinement of macromolecular structures by the maximum-likelihood method. *Acta Crystallogr D Biol Crystallogr* 53:240–255.
8. Perrakis A, Harkiolaki M, Wilson KS, Lamzin VS (2001) ARP/wARP and molecular replacement. *Acta Crystallogr D Biol Crystallogr* 57:1445–1450.
9. Virji M, et al. (1999) Critical determinants of host receptor targeting by Neisseria meningitidis and Neisseria gonorrhoeae: Identification of Opa adhesiotopes on the N-domain of CD66 molecules. *Mol Microbiol* 34:538–551.
10. Villullas S, Hill DJ, Sessions RB, Rea J, Virji M (2007) Mutational analysis of human CEACAM1: The potential of receptor polymorphism in increasing host susceptibility to bacterial infection. *Cell Microbiol* 9:329–346.
11. Cameron A, et al. (2004) Identification and activity of a series of azole-based compounds with lactate dehydrogenase-directed anti-malarial activity. *J Biol Chem* 279:31429–31439.
12. Konarev PV, Volkov VV, Sokolova AV, Koch MHJ, Svergun DI (2003) PRIMUS: A Windows PC-based system for small-angle scattering data analysis. *J Appl Crystallogr* 36:1277–1282.
13. Semenyuk AV, Svergun DI (1991) GNOM—a program package for small-angle scattering data processing. *J Appl Crystallogr* 24:537–540.
14. Franke D, Svergun DI (2009) DAMMIF, a program for rapid ab-initio shape determination in small-angle scattering. *J Appl Crystallogr* 42:342–346.
15. Volkov VV, Svergun DI (2003) Uniqueness of ab initio shape determination in small-angle scattering. *J Appl Crystallogr* 36:860–864.
16. Scholz T, et al. (2011) Processive behaviour of kinesin observed using micro-fabricated cantilevers. *Nanotechnology* 22:095707.
17. Hill DJ, Virji M (2003) A novel cell-binding mechanism of Moraxella catarrhalis ubiquitous surface protein UspA: Specific targeting of the N-domain of carcinoembryonic antigen-related cell adhesion molecules by UspA1. *Mol Microbiol* 48:117–129.
18. Meng G, Surana NK, St Geme JW, 3rd, Waksman G (2006) Structure of the outer membrane translocator domain of the Haemophilus influenzae Hia trimeric autotransporter. *EMBO J* 25:2297–2304.
19. Conners R, et al. (2008) The Moraxella adhesin UspA1 binds to its human CEACAM1 receptor by a deformable trimeric coiled-coil. *EMBO J* 27:1779–1789.
20. Sali A, Blundell TL (1993) Comparative protein modelling by satisfaction of spatial restraints. *J Mol Biol* 234:779–815.
21. Lovell SC, et al. (2003) Structure validation by Calpha geometry: phi, psi and C beta deviation. *Proteins* 50:437–450.

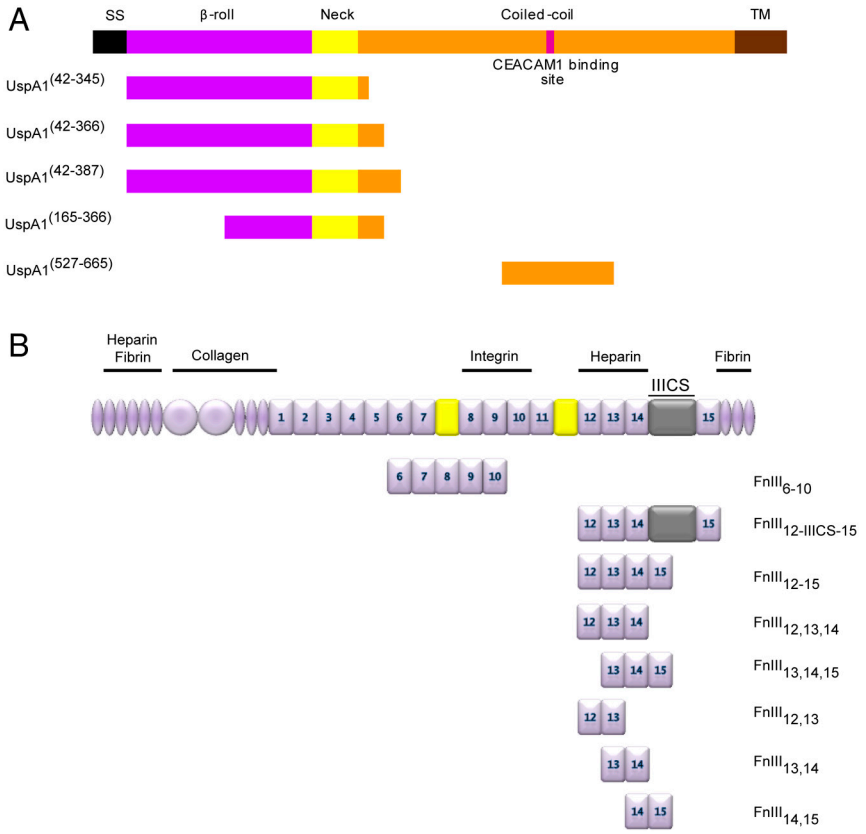

Fig. S1. Domain organization and truncated constructs of UspA1 and fibronectin. (*A*) Schematic showing full-length UspA1 comprises five regions. The signal sequence (SS) is highlighted in red, the β-roll head domain in blue, neck region in gold, coiled-coil stalk in green, and the transmembrane (TM) domain in brown. The CEACAM1-binding site is colored pink. The head domain constructs described in this study are shown below along with the previously structurally determined coiled-coil segment UspA1$^{(527–665)}$. (*B*) Fibronectin is composed of three different types of domains: type I (oval), type II (circle), and type III (rectangle). The common fibronectin domains (purple) are present in almost all variants, the extra type III modules (yellow) are splice variants present in cellular fibronectin but not plasma fibronectin. The type III connecting segment (IIICS, gray) is a site for integrin binding and varies greatly in length and presence. The domains implicated in binding important factors are indicated by a black line. The constructs derived from fibronectin in this study are displayed schematically at the bottom of the figure.

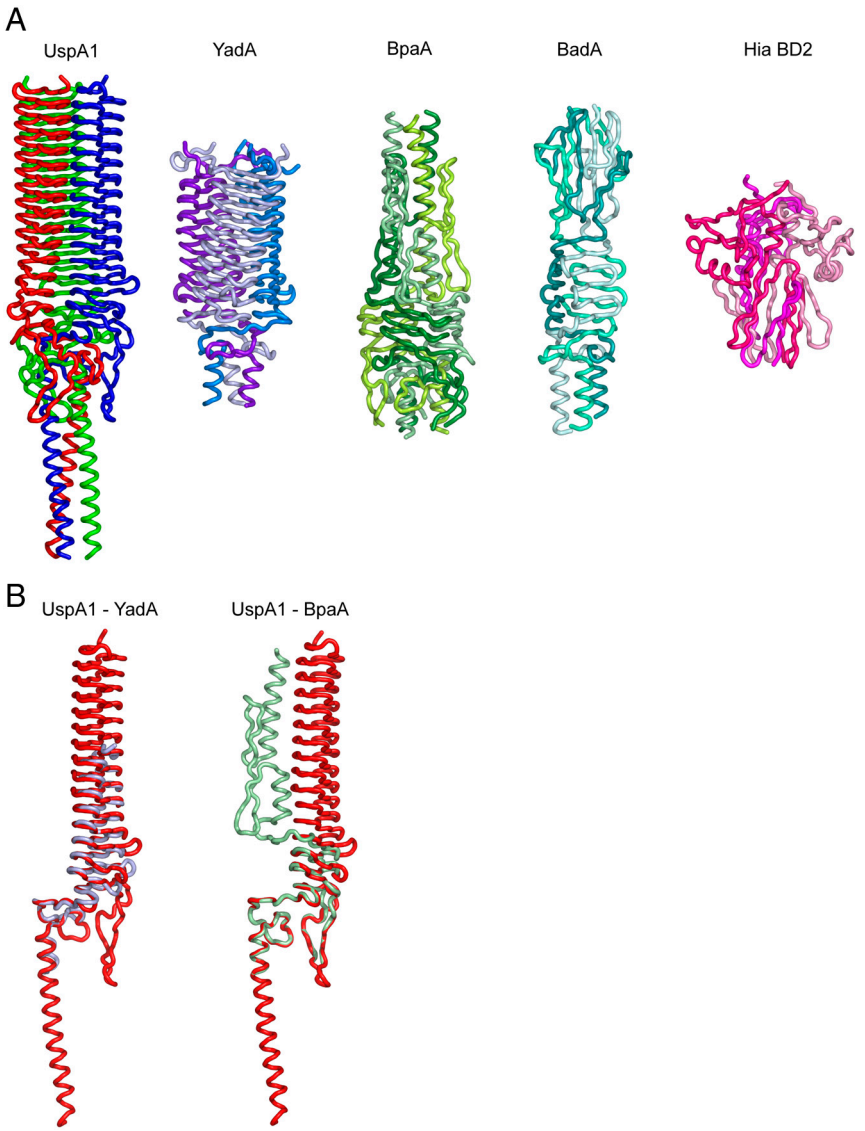

Fig. S2. Crystal structures of trimeric autotransporter adhesin head and neck domains. (*A*) UspA1 head domain structure compared to other bacterial adhesin head domains. (*B*) Overlay of a UspA1$^{(42–366)}$ monomer (green) with a YadA monomer (blue) to highlight the structural similarity within the head region, and of UspA1$^{(42–366)}$ (green) with BpaA (magenta) to highlight the structural similarity within the neck region.

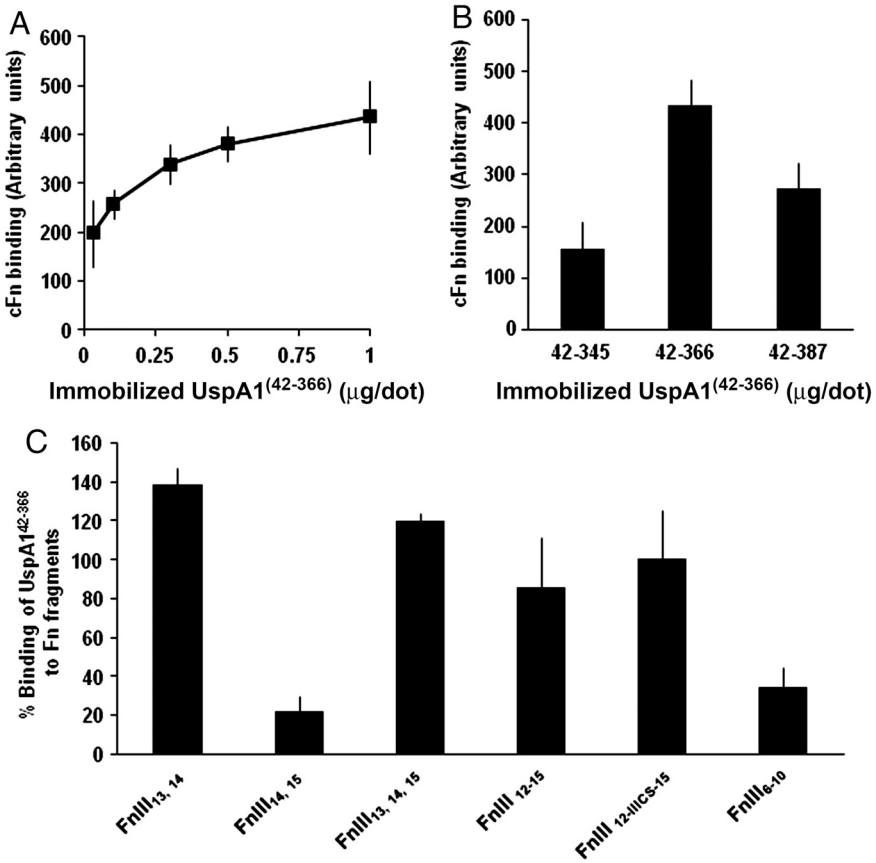

Fig. S3. Functional analysis of UspA1–fibronectin interaction by dot immunoblotting and ELISA. (*A* and *B*) Binding of human full-length cellular fibronectin (cFn) to truncated UspA1 fragments was quantified by densitometric analysis as described in *Materials and Methods*. (*A*) Binding of cFn overlaid at 3 μg/mL to increasing amounts of UspA1$^{(42–366)}$ dotted onto nitrocellulose. The bound Fn was detected using polyclonal anti-Fn antibody. (*B*) Relative binding of cFn to three UspA1 constructs [UspA1$^{(42–345)}$, UspA1$^{(42–366)}$, UspA1$^{(42–387)}$] was assessed similarly but using 1 μg/dot of each construct overlaid with 3 μg/mL cFn. Means of four independent experiments (each with duplicate or triplicate determinations) and errors are shown. (*C*) Binding of different fibronectin constructs (as shown) to UspA1$^{(42–366)}$ was assessed by dot immunoblotting as well as ELISA. In each case, UspA1$^{(42–366)}$ was immobilized on nitrocellulose (1 μg/dot) or coated onto Elisa plates (1 μg/well) and overlaid with fibronectin constructs (each used at 3 μg/mL). Binding was quantified as described in *Materials and Methods*. Both cFn and plasma Fn (pFn) were also used for comparison and their binding to UspA1$^{(42–366)}$ was found to be very similar. Percent binding of each Fn construct relative to that of full-length Fn is shown. Means of two to four independent dot immunoblotting and ELISA experiments (each with duplicate or triplicate determinations) and errors are shown.

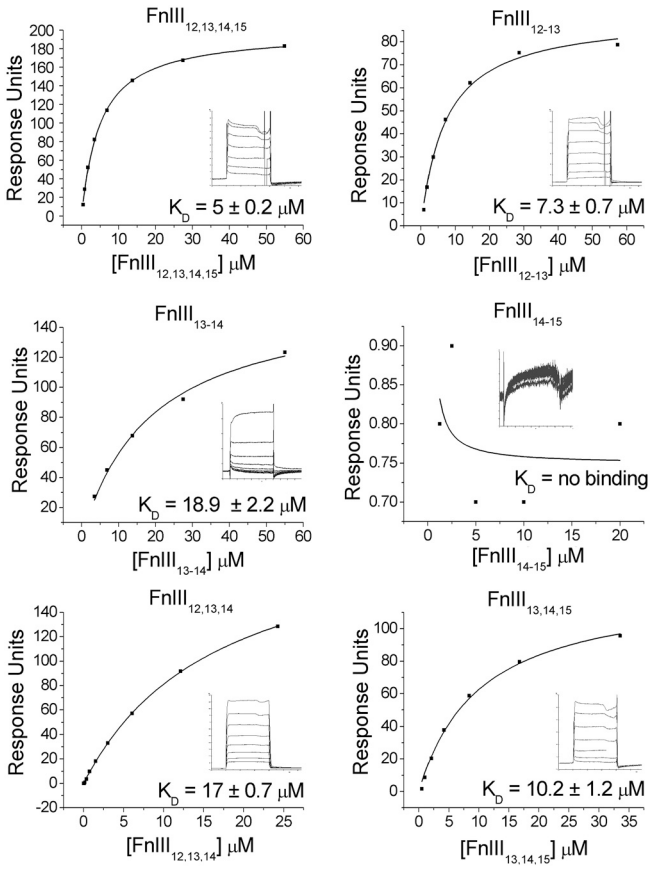

Fig. S4. Binding of fibronectin constructs to immobilized UspA1$^{(42–366)}$. Equilibrium binding analysis by surface plasmon resonance of soluble fibronectin constructs against UspA1$^{(42–366)}$. The estimated saturation level of the Fn constructs was calculated by nonlinear curve fitting. The K_d values are listed in Table S1. The inserts show the binding at different concentrations of soluble Fn constructs to UspA1$^{(42–366)}$.

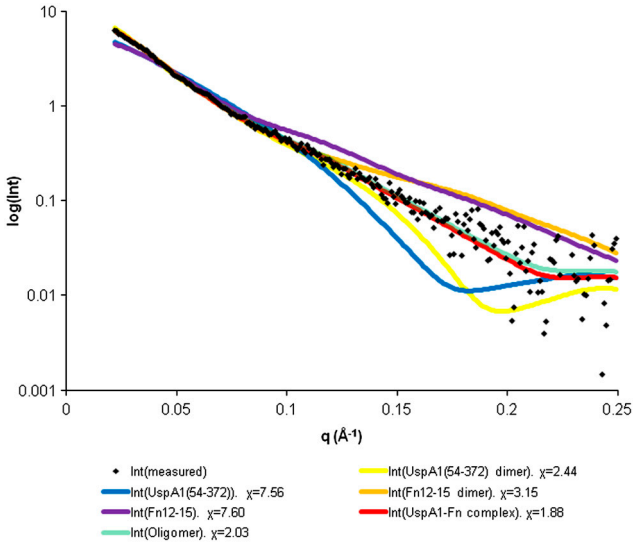

Fig. S5. SAXS analysis of UspA1$^{(42–366)}$-FnIII$_{12–15}$ complex. Experimental X-ray scattering intensity data for the UspA1$^{(54–372)}$-Fn$_{12–15}$ complex plotted in black as a function of q ($q = 4\pi \sin\theta/\lambda$, where 2θ is the scattering vector) and compared with theoretical scattering (solid lines) calculated from a representative rigid-body reconstruction of a UspA1$^{(54–372)}$ dimer (yellow), UspA1$^{(54–372)}$ monomer (blue), Fn$_{12–15}$ dimer (orange), Fn$_{12–15}$ monomer (purple), and UspA1$^{(54–372)}$-Fn$_{12–15}$ (red). For each model, χ values showing goodness-of-fit to the experimental data are given in the key. It can clearly be seen that only the UspA1$^{(54–372)}$-Fn$_{12–15}$ complex is in good agreement with the experimental data. The green line shows the theoretical scattering intensity calculated by the OLIGOMER software, when fitting a variable mixture of the UspA1$^{(54–372)}$ – Fn$_{12–15}$ complex (87.5%) and each of the components (12.5%).

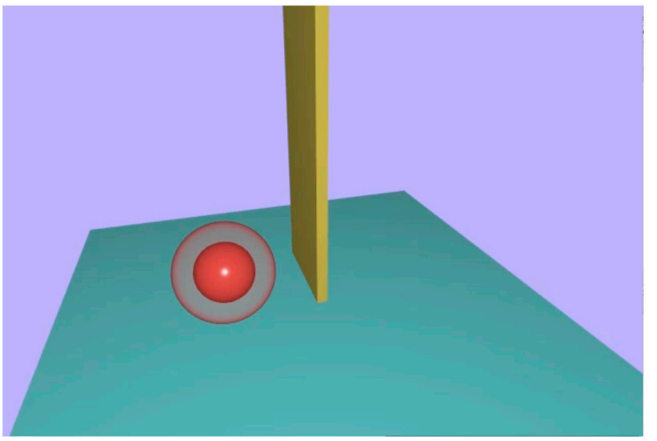

Movie S1. Schematic showing the LMFM arrangement with a single *Mx* bacterium. The movie shows movement of the stage containing a single *Mx* bacterium toward the vertically mounted probe. The point of contact with the probe and its resulting deflection are measured to provide both spatial and force response information.
Movie S1 (AVI)

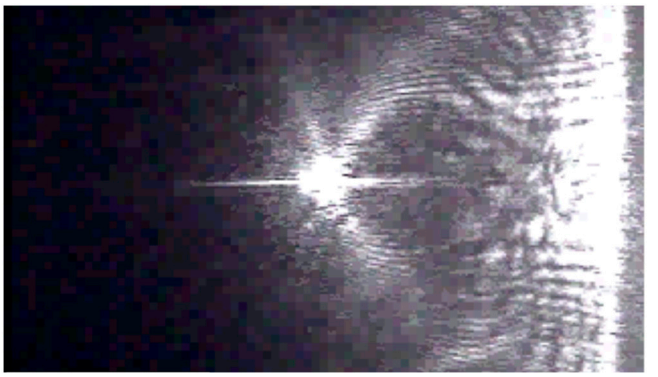

Movie S2. Representative data showing LMFM analysis of a single *Mx* bacterium in the absence of receptors. Derived data equivalent to that in Fig. 2*B*.
Movie S2 (MOV)

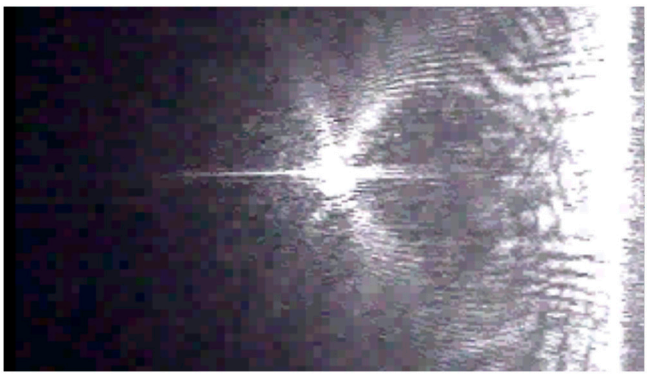

Movie S3. Representative data showing LMFM analysis of a single *Mx* bacterium in the presence of CEACAM1 receptor. Derived data equivalent to that in Fig. 2*C*.
Movie S3 (MOV)

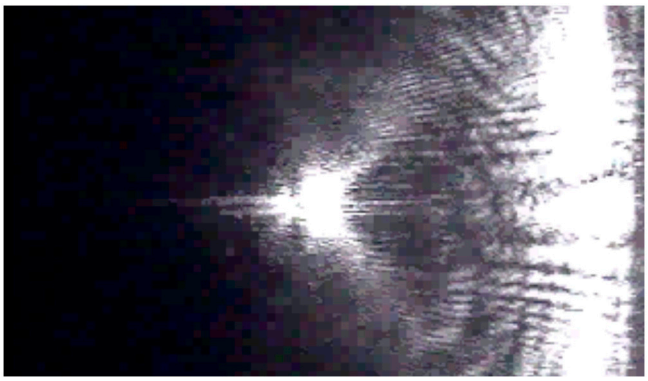

Movie S4. Representative data showing LMFM analysis of a single *Mx* O35E bacterium in the presence of CEACAM1 receptor. The O35E strain of *Mx* lacks a CEACAM1 binding site and hence, despite the presence of the CEACAM1 receptor, data derived from these experiments does not differ significantly from *Mx* with buffer/control or no receptor.

Movie S4 (MOV)

Table S1. Summary of binding affinity constants between Fn constructs and UspA1$^{(42–366)}$

Fn construct	UspA1$^{(42–366)}$
FnIII$_{12,13}$	7.3 ± 0.7 mM
FnIII$_{13,14}$	18.9 ± 2.2 μM
FnIII$_{14,15}$	no binding detected
FnIII$_{12,13,14}$	17 ± 0.7 μM
FnIII$_{13,14,15}$	10.2 ± 1.2 μM
FnIII$_{12,13,14,15}$	5.0 ± 0.2 μM

Table S2. Summary of X-ray diffraction data and refined model statistics for UspA1$^{(153–366)}$ and UspA1$^{(42–345)}$

	UspA1$^{(153–366)}$	UspA1$^{(153–366)}$ NaBr soak	UspA1$^{(153–366)}$ NaBr soak	UspA1$^{(42–345)}$
Diffraction data				
Wavelength, Å	0.97630	0.92094 (peak)	0.92114 (inflection)	0.9765
Resolution range, Å	100–2.20 (2.28–2.20)	43.76–2.55 (2.69–2.55)	43.81–2.55 (2.69–2.55)	102.38–2.94 (3.01–2.94)
Space group	$P2_1$	$P6_3$	$P6_3$	$P6_3$
Unit cell	$a = 50.30$ Å $b = 142.85$ Å $c = 50.27$ Å $\alpha = \gamma = 90°$ $\beta = 119.96°$	$a = b = 50.53$ Å $c = 143.56$ Å $\alpha = \beta = 90°$ $\gamma - 120°$	$a = b = 50.59$ Å $c = 143.70$ Å $\alpha = \beta = 90°$ $\gamma = 120°$	$a = b = 118.22$ Å $c = 176.57$ Å $\alpha = \beta = 90°$ $\gamma = 120°$
Completeness, %	98.5 (93.9)	100 (100)	100 (100)	99.85 (95.3)
Total no. unique reflections	31,153 (2,903)	6,811 (979)	6,831 (985)	29,914 (2,117)
Redundancy	3.4 (2.6)	24.4 (6.6)	21.4 (5.2)	12.3 (8.7)
$I/\sigma I$	11.6 (1.4)	42.8 (41.9)	42.7 (41.7)	16.3 (3.4)
R_{sym}*	0.086 (0.552)	0.160 (0.789)	0.198 (1.097)	0.116 (0.707)
Wilson B factor	34.1	45.0	46.8	77.5
Refinement statistics				
Total no. of reflections	29,082 (1,921)			28,193 (2,075)
No. of reflections in test set	1,543			1,503
R_{cryst}†	0.182 (0.281)			0.2026 (0.299)
R_{free}	0.244 (0.313)			0.2162 (0.313)
rmsd: bond lengths, Å	0.019			0.0076
rmsd: bond angles, °	1.680			1.040
rmsd: bonded B factors—main chain	0.55			0.501
RMSD: bonded B factors—side chain	1.72			1.95
Protein atoms	4,568			6,132
Solvent molecules	172			45
Ligands				
Ni^{2+}	1			
Cl^-	1			
SO_4	3			
B average, protein, Å^2	26.8			25.82
Ramachandran plot, favored, %	96			96.2

Values in parentheses are the statistics for the highest resolution shell.

*$R_{sym} = \Sigma_{hkl}\Sigma_i|I_i(hkl) - \langle I(hkl)\rangle|/\Sigma_{hkl}\Sigma_i I_i(hkl)$.

†$R_{cryst} = \Sigma_{hkl}|F_o(hkl) - F_c(hkl)|/\Sigma_h|F_o(hkl)|$. The refined model was validated using MOLPROBITY (21).